fibers

MDPI

Article

Hydration and Water Vapor Transport in Films Based on Cassava Starch Reinforced with Topinambur Fiber (*Helianthus tuberosus*)

Luisa F. Sierra Montes [1,2], María C. Lorenzo [3,4], Maria A. García [1,2], Andrés G. Salvay [5,*] and Laura Ribba [6,7,*]

1 Centro de Investigación y Desarrollo en Ciencia y Tecnología de los Alimentos (CIDCA), Universidad Nacional de La Plata (UNLP), Consejo Nacional de Investigaciones Científicas y Técnicas (CONICET), Comisión de Investigaciones Científicas (CICPBA), 47 y 116, La Plata B1900AJJ, Argentina; luisaf.2294@gmail.com (L.F.S.M.); magarcia@quimica.unlp.edu.ar (M.A.G.)
2 Facultad de Ciencias Exactas, Universidad Nacional de La Plata (UNLP), 47 y 115, La Plata B1900AJJ, Argentina
3 Instituto Nacional de Tecnología Industrial (INTI) Plásticos, Av. Gral. Paz 5445, San Martín B1650WAB, Argentina; clorenzo@inti.gob.ar
4 Instituto de Ingeniería Ambiental, Escuela de Hábitat y Sostenibilidad, Universidad Nacional de San Martín, San Martín, Buenos Aires B1650WAB, Argentina
5 Departamento de Ciencia y Tecnología, Universidad Nacional de Quilmes (UNQ), Roque Sáenz Peña 352, Bernal B1876BXD, Argentina
6 Instituto Nacional de Tecnología Industrial (INTI) Plásticos, Consejo Nacional de Investigaciones Científicas y Técnicas (CONICET), San Martín B1650WAB, Argentina
7 Departamento de Física, Facultad de Ciencias Exactas y Naturales, Universidad de Buenos Aires (UBA), Buenos Aires C1428EGA, Argentina
* Correspondence: asalvay@unq.edu.ar (A.G.S.); lribba@inti.gob.ar (L.R.)

Abstract

Biodegradable composites obtained by reinforcing thermoplastic starch (TPS) with lignocellulosic fibers show great potential, but their strong sensitivity to water still limits practical applications. Among possible reinforcements, *Helianthus tuberosus* (topinambur) represents an underutilized agricultural residue that has been scarcely explored in this context. In this work, we demonstrate for the first time that topinambur fiber can improve the water vapor barrier properties of cassava starch films, while also providing a detailed analysis of sorption isotherms and the humidity-dependent relationship between surface roughness and contact angle, aspects rarely addressed in previous studies. SEM revealed uniform fiber dispersion and integration. Water sorption kinetics showed that fiber addition reduces both hydration and sorption time constant, indicating lower water affinity and greater water mobility. Water sorption isotherms confirmed that fiber incorporation significantly alters overall hydration and water–matrix interactions, revealing reduced effective water solubility in films. Water vapor permeability also decreased with fiber addition, mainly due to decreased water solubility, rather than changes in water diffusivity. While fiber addition enhanced surface-water repellency across all humidity levels, roughness exhibited a humidity-dependent response FTIR analysis confirmed fiber–matrix compatibility and suggested new hydrogen bonding. Overall, these findings identify topinambur fiber as a novel reinforcement for designing biodegradable films with improved humidity resistance for agroecological applications.

Keywords: biodegradable films; topinambur fiber; hydration; water vapor permeability; film surface properties; film morphology

check for updates

Academic Editor: Martin J. D. Clift

Received: 11 August 2025
Revised: 30 September 2025
Accepted: 9 October 2025
Published: 15 October 2025

Citation: Sierra Montes, L.F.; Lorenzo, M.C.; García, M.A.; Salvay, A.G.; Ribba, L. Hydration and Water Vapor Transport in Films Based on Cassava Starch Reinforced with Topinambur Fiber (*Helianthus tuberosus*). *Fibers* **2025**, *13*, 141. https://doi.org/10.3390/fib13100141

Copyright: © 2025 by the authors. Licensee MDPI, Basel, Switzerland. This article is an open access article distributed under the terms and conditions of the Creative Commons Attribution (CC BY) license (https://creativecommons.org/licenses/by/4.0/).

1. Introduction

The global production of bioplastics is experiencing notable growth, with annual rates projected to exceed 15%, reaching approximately 2.4 million tons by 2022. Despite this expansion, bioplastics currently account for under 1% of the world's plastic output, highlighting the urgent need to accelerate their adoption in key sectors such as agriculture [1,2]. This sector alone consumes around 6.6 million tons of plastics annually, and this figure is expected to rise by 64% by 2030 to meet the challenges posed by population growth and climate change impacts on food systems [3].

Plastic materials are widely employed in agriculture to enhance productivity and resource efficiency. Common uses include greenhouse films, mulching, irrigation systems, seedling trays, and packaging. These applications help retain soil moisture, stabilize temperature, control weeds, and reduce water evaporation [4]. However, the prevalent use of non-biodegradable plastics such as polyethylene (PE), polypropylene (PP), and polystyrene (PS) has raised environmental concerns. These materials tend to fragment under environmental exposure, releasing microplastics into soils and waterways, where they may persist for decades and enter food chains [5–7]. Thus, there is a growing demand for alternative biodegradable materials that are not only renewable but also minimize the risks associated with microplastic pollution.

Among the available options, thermoplastic starch (TPS) stands out as a promising candidate. It is biodegradable, renewable, non-toxic, and cost-effective [8,9]. However, TPS suffers from high sensitivity to humidity and limited mechanical strength, primarily due to the abundance of hydrophilic hydroxyl groups in starch chains [10,11]. To address these limitations, reinforcing TPS with natural fibers has gained increasing attention, offering a green route to improve mechanical and barrier properties without compromising biodegradability [12].

Topinambur (*Helianthus tuberosus*) is a perennial species originally from North America, well known for its adaptability to harsh conditions such as drought and frost. While its tuber is cultivated for food and bioethanol production, the aerial parts are typically discarded despite their rich lignocellulosic composition [13,14]. This biomass residue has a lignocellulosic content close to 87%, with about 41% cellulose, 14% hemicellulose and 24% lignin -making it an attractive reinforcement candidate for biobased materials [15]. Previous work from our group demonstrated that the incorporation of 10 wt% topinambur fiber into cassava starch-based TPS films increased the Young's modulus by 70%, with no significant impact on biodegradability [15]. However, beyond mechanical enhancement, behavior related to hydration and water transport remains a key challenge for TPS-based materials.

Biopolymeric materials, such as films based on TPS are highly hydrophilic and readily absorb moisture, a feature that strongly influences their storage stability, shelf life, and overall performance in real-world applications [16]. The presence of hydration water is crucial in determining both structural integrity and functional behavior of these matrices [16].

Acting in a plasticizing manner, water molecules penetrate between polymer chains, increasing the free volume, lowering the glass transition temperature (T_g), and enhancing flexibility [17,18]. The moisture level within the films is governed by the relative humidity (RH) of the surrounding environment [16,19,20]. Sorption isotherms, which relate equilibrium water content to environmental RH, offer valuable information about film–water interactions and the distribution of absorbed water inside the matrix [19,21]. Consequently, the mechanical performance and other physical characteristics of hydrophilic biopolymers are strongly conditioned by the prevailing ambient humidity [16,22].

Moreover, hydration water is closely linked to the water vapor transport properties of hydrophilic films [21,23,24]. The water vapor permeability is a critical characteristic of biopolymer-based films, as it determines their capacity to regulate moisture exchange

between a system and its surroundings [23]. In hydrophilic materials like TPS-based films, the strong interaction with water molecules results in poor water vapor barrier performance [25]. In these films, water transport proceeds not via pore channels but instead follows a sorption–diffusion–desorption mechanism [21,26–28]. Therefore, water vapor permeability is affected by both the hydration level and solubility of water in the film, together with the molecular mobility of water inside the matrix [26].

Previous studies have shown that the joint analysis of sorption isotherms and vapor permeability allows distinguishing between water solubility and diffusion effects, providing a more comprehensive understanding of water transport in hydrophilic polymeric systems [21]. Factors such as film thickness [20,21,28–30], water vapor pressure gradient [21,27,31,32], and plasticizer content [28,33,34] can significantly influence water vapor permeability in biopolymer-based materials. Additionally, some authors have reported a slight reduction in water vapor permeability upon incorporating cellulose nanoparticles into starch films, which has been attributed to the creation of a more tortuous diffusion path [35]. On the other hand, significant changes in the water vapor permeability of yeast biomass-based films have been observed when reinforced with rice husk cellulose nanofibers [36]. However, in that study, the authors did not investigate the hydration behavior of the films, nor did they examine how the solubility of water in the material and the diffusion of water contribute to permeability.

While several studies have explored the reinforcement of thermoplastic starch with lignocellulosic fibers, the majority focus on mechanical or thermal performance [15,37–39]. Reports examining hydration kinetics, water sorption isotherms, and water transport phenomenon in detail specifically through the contributions of water solubility and diffusion within the film are scarce. Moreover, to the best of our knowledge, no previous work has systematically evaluated how environmental humidity influences surface roughness in fiber-reinforced TPS films using contact profilometry. In addition, the effect of incorporating topinambur fibers on the barrier properties of TPS films has never been investigated.

The present study addresses these gaps for the first time through an evaluation of the water-related properties of cassava starch-based films reinforced with varying contents of fibers from the aerial part of *Helianthus tuberosus*. In particular, we analyze how fiber content affects water solubility and diffusion within the films. We also assess changes in surface morphology, roughness, and hydrophobicity under different relative humidity conditions. Additionally, FTIR spectroscopy is employed to examine molecular interactions between fiber and matrix, providing insight into compatibility and hydrogen bonding. The combination of these complementary characterizations offers a comprehensive understanding of moisture transport and surface response in TPS-based materials reinforced with natural fibers, aiding the design of tailored formulations for agricultural uses such as mulch films or controlled-release systems.

2. Materials and Methods

2.1. Materials

Cassava starch, sourced from Aldema Cooperative (Misiones, Argentina) and topinambur aerial crop residues (stems) from the Faculty of Agronomy (UNLP) cultivated in La Plata City (Buenos Aires, Argentina, (34°56′ S, 57°57′ W) were utilized. Topinambur stems were ground into powder using a high-speed multifunction grinder (Damai HC-250Y, Xinchang, Shaoxing, Zhejiang, China), followed by sieving through a 500 µm mesh (ALEIN International, Argentina) to ensure a limited maximum particle size. Topinambur fiber was stored in airtight flasks until used. Analytical grade glycerol and sorbitol (Anedra, Buenos Aires, Argentina) were used as plasticizers. Silica gel, and all salts used were obtained from Biopack (Buenos Aires, Argentina).

2.2. Preparation of the Biocomposite Films

Cassava starch and topinambur fiber-reinforced films were obtained by extrusion and thermo-compression. Initially, the material was processed into pellets using a single-screw extruder Brabender OHG (Duisburg, Germany). These pellets were then used to produce films by thermo-compression in a hydraulic press Smaniotto (Buenos Aires, Argentina). Formulations were prepared using starch (70%), sorbitol (10%), glycerol (10%), and distilled water (10%, *w*/*w*), with topinambur fibers added at 0, 5, or 10% relative to starch. The systems were processed at a barrel temperature profile of 85, 100, 110, 115, 125 °C at 70 rpm. Compression molding was conducted at 130 °C with pressures of 40, 110, and 160 bar for a total of 15 min, followed by cooling under pressure for 10 min. To ensure consistent film thickness, 24 g of material were placed in a standardized 20 × 20 cm mold for each sample. For clarity, the formulations were labeled as follows: TPS for the neat matrix, TPS–TOPI5% for films with 5% fiber, and TPS–TOPI10% for those with 10% fiber. In a previous study [15], fiber contents ranging from 0 to 20 wt% (starch basis) were tested. However, concentrations above 10 wt% induced defects in the TPS matrix and processing difficulties. Therefore, in the present work the fiber content was limited to 5 and 10 wt%. Prior to characterization, the films were equilibrated at 25 °C and 60% relative humidity.

2.3. Films Characterization

2.3.1. Scanning Electron Microscopy (SEM)

The microstructure of the films was examined using a Phenom ProX scanning electron microscope (Phenom World, Atlanta, GA, USA) operating under low vacuum conditions. Film samples were immersed in liquid nitrogen and cryo-fractured to expose the cross-section, then mounted on bronze stubs using double-sided carbon adhesive tape. The specimens were sputter-coated with a thin film of platinum and observed at 150× and 2000× magnification using an accelerating voltage of 5 kV.

2.3.2. Thickness Measurements and Density of the Films

Thickness measurements were conducted at 20 distinct locations on each film using a digital caliper ($\pm 10^{-6}$ m; 3109-25-E, Insize Co., Suzhou, China), resulting in an average thickness of (0.43 ± 0.01) mm per specimen. To determine the dry-basis film density ($\rho_{d.b.}$, g m^{-3}), circular samples with an area of 44 cm^2 were dried to constant weight in desiccators containing silica gel (≈0% RH) for 15 days. During film dehydration, the silica gel was not replaced because no hydration of the desiccant was observed, as evidenced by the absence of any color change in the gel. An analytical balance (accuracy ± 10^{-4} g) was employed to measure the mass of the films. $\rho_{d.b.}$ was calculated according to Equation (1):

$$\rho_{d.b.} = \frac{DM}{A \times L}, \quad (1)$$

where DM is the dry mass (g), A the area (m^2), and L the film thickness (m).

2.3.3. Kinetics of Water Sorption

Water vapor sorption kinetics experiments for the films were conducted in triplicate at 22 °C. Circular samples with a diameter of 75 mm were previously dried in an environment containing silica gel for 15 days. Subsequently, they were then placed in sorption containers maintained at 90% RH using a saturated $BaCl_2$ solution. The samples were weighed at specific time intervals with an analytical balance ($\pm 10^{-4}$ g) to collect data. The water content h in g H_2O per g of dried mass (DM) was evaluated taking the difference between the mass of the hydrated film and that of the fully dried film. For each sample formulation, a water sorption kinetics curve was obtained, and the water content h at each sorption time

t was calculated as the mean of three independent experimental measurements, along with their corresponding errors. The relationship between h and t was fitted using a first-order kinetics model [40], employing a bi-exponential function that accounts for two distinct water uptake rates, as shown in Equation (2):

$$h(t) = h_0 + \Delta h_1 \left[1 - exp\left(-\frac{t}{\tau_1}\right)\right] + \Delta h_2 \left[1 - exp\left(-\frac{t}{\tau_2}\right)\right], \quad (2)$$

where h_0 is the initial water content ($h_0 = 0$), Δh_1 and Δh_2 are the water content associated with the contribution of processes 1 and 2, respectively, and τ_1 and τ_2 are time constants for the water uptake of each process. The equilibrium water content at 90% RH, h_∞, was calculated as $h_\infty = \Delta h_1 + \Delta h_2$. The average time constant τ for the entire water uptake process was calculated as $\tau = \left(\frac{\Delta h_1}{h_\infty}\right)\tau_1 + \left(\frac{\Delta h_2}{h_\infty}\right)\tau_2$, where $\Delta h_1/h_\infty$ and $\Delta h_2/h_\infty$ represent the proportions of the contribution to the total hydration from processes 1 and 2, respectively. The parameters Δh_1, Δh_2, τ_1 and τ_2, along with their corresponding errors, were determined by fitting the experimental data to Equation (2) using OriginPro 8 (OriginLab Corporation, Northampton, MA, USA).

2.3.4. Water Sorption Isotherms

Water sorption isotherms were assessed gravimetrically at 22 °C, following the standard methodology previously outlined [17]. Temperature influences water sorption isotherms by affecting a material's capacity to absorb and release water. In general, for food and many other materials, an increase in temperature leads to a reduction in moisture content at the same relative humidity, causing the sorption curves to shift toward lower moisture levels [41]. This behavior occurs because higher temperatures enhance molecular mobility and favor the vapor phase. In this study, a temperature of 22 °C was selected as representative, as it lies between low and high temperature conditions. Dried film specimens, each with a surface area of 44.2 cm^2, were placed in 3 L desiccators under various water activity a_w (a_w = % RH/100) conditions. Saturated solutions of NaOH, $MgCl_2$, K_2CO_3, NaBr, NaCl, and $BaCl_2$ were employed to generate a_w conditions of 0.10, 0.33, 0.43, 0.57, 0.75, and 0.90, respectively. Silica gel was used to create a dry atmosphere (≈0% RH). Moisture sorption was tracked by periodically determining the sample mass with an analytical balance ($\pm 10^{-4}$ g) at each a_w, continuing until no further change in weight was observed. Hydration or water content (h) was expressed as g of water per g of dry matter (DM) and plotted as a function of a_w. Each measurement was performed three times, and the sorption isotherm data were fitted to the Guggenheim–Anderson–de Boer (GAB) model [19], as detailed in Equation (3):

$$h(a_w) = \frac{Nck\, a_w}{[(1 + (c-1)\, ka_w)](1 - k\, a_w)}, \quad (3)$$

where N represents the monolayer water content (g of water per g of dry matter), corresponding to the primary binding sites for hydration water molecules. The parameter c is related to the sorption heat of the monolayer, reflecting the strength of water binding to the primary binding sites, while k is associated with the sorption heat of the multilayer, indicating the capacity of water to bind within the multilayer structure [19]. For each sample formulation, a single water sorption isotherm was obtained, and the water content (h) at each water activity (a_w) was calculated as the mean of three experimental measurements, including their respective errors. The parameters N, c, and k, along with their corresponding errors, were determined by fitting the experimental data to the GAB model using OriginPro 8 (OriginLab Corporation, Northampton, MA, USA).

2.3.5. Experimental Water Vapor Permeability Measurements

The films' experimental water vapor permeability (P_w^{exp}) was measured according to the ASTM E96 (2016) cup method [42], with minor adjustments following [28]. In brief, films were sealed over cups containing a saturated $BaCl_2$ solution, creating a high RH environment of 90%. These cups were then placed inside 7 L desiccators maintained at 22 °C and 10% RH provided by a saturated NaOH solution. To promote uniform environmental conditions within the desiccators and across the film surfaces, air circulation was provided by a fan, as suggested in previous studies [28]. The weight loss of the cups (m_{H_2O}), representing the amount of water vapor transmitted through the films, was monitored using an analytical balance ($\pm 10^{-3}$ g). m_{H_2O} was plotted as a function of the time t, and once a steady state (evidenced by a linear relationship) was achieved, measurements were continued for an additional 30 h. Water vapor flux (J_w) was determined taking the slope ($\Delta m_{H_2O}/\Delta t$) from the linear fit of sample weight loss as a function of time by Equation (4):

$$J_w = \frac{1}{A}\left(\frac{\Delta m_{H_2O}}{\Delta t}\right), \quad (4)$$

where A is the exposed area of the film (2.2×10^{-3} m^2). The experimental water vapor permeability P_w^{exp} was calculated according to Equation (5):

$$P_w^{exp} = \left(\frac{J_w L}{\Delta p_w}\right), \quad (5)$$

where P_w^{exp} is given in units of g s^{-1}m^{-1}Pa^{-1}, L is the film thickness, and $\Delta p_w = (p_{w2} - p_{w1})$ is the differential water vapor partial pressure across the film. p_{w1} and p_{w2} are the partial pressures (Pa) of water vapor at the film surface outside and inside the cup, respectively. Experiments were conducted in triplicate.

2.3.6. Evaluation of Effective Water Solubility and Diffusion in the Films

Experimental water vapor permeability in hydrophilic biopolymer films is defined as [26]:

$$P_w^{exp} = D_w^{eff} S_w^{eff}, \quad (6)$$

where S_w^{eff} (g m^{-3} Pa^{-1}) is the effective water solubility coefficient over the water concentration range C_{w2} to C_{w1}, corresponding to water vapor pressures p_{w2} and p_{w1}, respectively, and D_w^{eff} (m^2 s^{-1}) is the effective diffusion coefficient over C_{w2} to C_{w1}. Water sorption isotherms were employed to estimate the water concentration C_w ($C_w = h(a_w) \times \rho_{d.b.}$) on the surface of each film sample in the permeability experiment. S_w^{eff} corresponding to the pressure gradient or a_w interval $a_{w2} = 0.9$ to $a_{w1} = 0.1$ was obtained by Equation (7) [21]:

$$S_w^{eff} = [(h(a_{w2}) - (h(a_{w1}))/(p_{w2} - p_{w1})]\rho_{d.b.}, \quad (7)$$

where $h(a_{w2})$ and $h(a_{w1})$ denote the water content of the film at the bottom surface (p_{w2}) and the surface outside the cup (p_{w1}). According to Equation (6), D_w^{eff} was calculated as

$$D_w^{eff} = P_w^{exp} / S_w^{eff}. \quad (8)$$

2.3.7. Film Surface Roughness and Contact Angle

Surface roughness and static contact angle of neat TPS and TPS–TOPI5% and TPS–TOPI10% were measured after conditioning the films during 7 days at 20 °C at 0% (silica gel), 10% (NaOH saturated solution), 43% (K_2CO_3 saturated solution), and 90% ($BaCl_2$ saturated solution) relative humidity. Surface roughness parameters, Ra (average roughness) and Rz

(mean peak-to-valley height), were measured with a PCE-RT 1200 profilometer (Schwyz, Switzerland). A minimum of 15 readings were collected for each sample. Film samples were also observed in a Leica S8AP0 stereomicroscope equipped with a Leica MC170 HD camera (Mannheim, Germany).

To study the wettability of the materials' surface, previously conditioned as described, the contact angle was determined using a Ramé-hart Model 190 goniometer (Ramé-hart Instrument Co., Succasunna, NJ, USA). For each sample, at least 10 measurements were performed.

2.3.8. Fourier Transform Infrared Spectroscopy (FTIR)

The FTIR characterization of the films was performed on a Nicolet iS10 (Thermo Scientific, Madison, WI, USA) coupled to an Attenuated Total Reflectance (ATR) accessory. Each spectrum was recorded between 4000 and 400 cm^{-1}, with 32 scans averaged per sample at a resolution of 4 cm^{-1}.

2.3.9. Small- and Wide-Angle X-Ray Scattering (SAXS/WAXS)

Measurements were performed in parallel-beam transmission geometry using a SAXS/WAXS Xeuss 2.0 XENOCS UHR HP200 (Xenocs, Grenoble, France) instrument (Laboratorio de Cristalografía Aplicada, ITECA Institute, CONICET–Universidad Nacional de San Martín, Argentina), following the methodology reported by [43] with minor modifications. The system is equipped with a microfocus Cu-Kα GeniX^{3D} X-ray tube and two Dectris Pilatus3R hybrid photon-counting detectors: a 200K-A detector for SAXS, positioned 335 mm from the sample, and a 100K detector for WAXS, located 158 mm away at a fixed angle of 36°. This configuration provided a combined 2θ range of 0.5–45°. High-resolution optics with a beam spot size of 500 × 500 µm was used.

2.4. Statistical Analysis

Statistical processing was carried out using InfoStat 2020. Comparisons between groups were assessed through analysis of variance (ANOVA), followed by Fisher's LSD test (α = 0.05). Data are presented as means ± standard deviation. The errors in the parameters obtained from the bi-exponential and GAB models, derived from the water sorption kinetics curves and water sorption isotherms, respectively, were estimated via the fit analysis.

3. Results and Discussion

3.1. Microstructural Characterization of Films

Figure 1 shows SEM micrographs of cryo-fractured cross-sections of cassava starch-based films reinforced with increasing amounts of topinambur fiber. The unreinforced TPS film (Figure 1a) exhibits a relatively smooth and continuous morphology, with occasional rounded features attributed to residual ungelatinized starch granules. No signs of phase separation or structural discontinuities are observed, indicating a homogeneous TPS matrix.

Upon the addition of 5 wt% fiber (Figure 1b), the cross-section becomes more irregular, with the appearance of dispersed particulate features throughout the matrix. These are attributed to the embedded topinambur fibers and suggest good dispersion of the filler at this concentration. However, some local agglomeration is observed, possibly related to the fibrous nature of the filler.

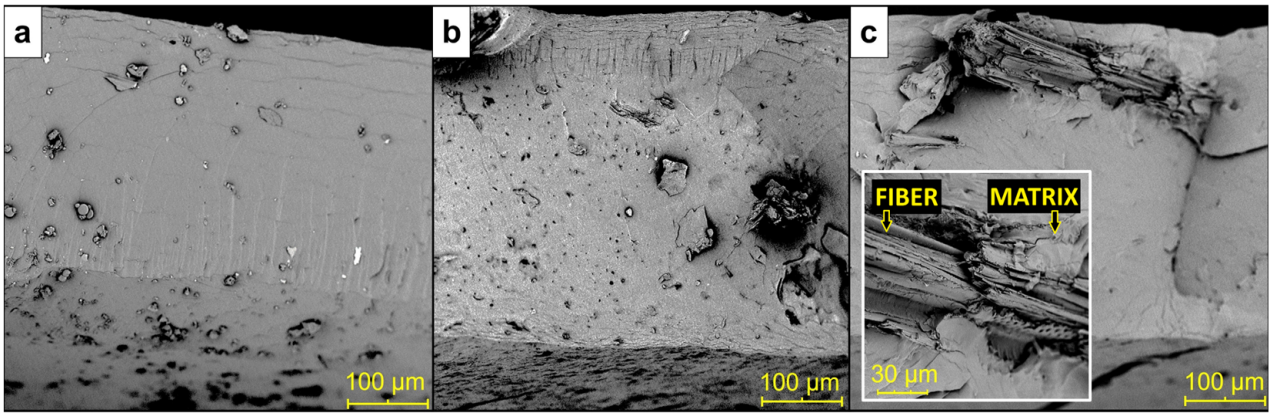

Figure 1. SEM images of cassava starch-based films cryofractured cross-section: (**a**) TPS, (**b**) TPS–TOPI5%, and (**c**) TPS–TOPI10%. Images captured at 150× and 2000×.

In the film containing 10 wt% fiber (Figure 1c), the filler content is significantly higher, and clusters of elongated structures become visible. These features are clearly discernible in the inset, where bundles of cellulose-rich fibers are embedded within the TPS matrix. The fiber–matrix interface appears continuous, with no evident voids or detachment. Although SEM analysis alone does not provide definitive evidence of interfacial adhesion, the observed morphological continuity suggests a good level of compatibility between the components. Similar microstructural behavior has been reported in other TPS-based composites reinforced with lignocellulosic residues [44].

Overall, SEM observations confirm that the topinambur fiber is successfully embedded within the TPS matrix, with improved integration and distribution as fiber content increases. The well-integrated interface observed at 10% filler content is expected to play a key role in modulating both mechanical and water-related properties.

3.2. Water Vapor Sorption

Figure 2a, shows the kinetics of water sorption at 90% RH for dehydrated TPS films and topinambur fiber-reinforced films at 5 and 10% filler content. The experimental data were fitted using a first-order bi-exponential kinetics model (Equation (2)), with the corresponding parameters presented in Table 2. This model considers two hydration processes: a faster one (process 1) and a slower one (process 2). Figure 2a, reveals that the hydration water content (h) decreased with increasing topinambur fiber content in the films. Therefore, the addition of topinambur fiber to TPS enhances the overall hydrophobicity of the material. As shown in Table 2, the incorporation of topinambur fiber results in a notable reduction in the equilibrium hydration at 90% RH (h_∞), along with a decrease in the average time constant (τ) for the overall water uptake process. These results indicate that incorporating topinambur fiber into the TPS matrix reduces hydration, allowing water molecules to be sorbed and mobilized more rapidly, thus reaching equilibrium moisture content faster. A significant reduction in equilibrium hydration under high humidity conditions was likewise detected at a comparable temperature in TPS reinforced with winceyette fibers [45]. However, the influence of fiber content on the equilibrium water content of these materials was not evident [45]. Additionally, a smaller reduction in the equilibrium hydration at high humidity was observed in composites of potato starch reinforced with 10% cellulose and 10% hemp fibers, whereas no changes were detected when potato starch was reinforced with 10% wheat straw fibers [46].

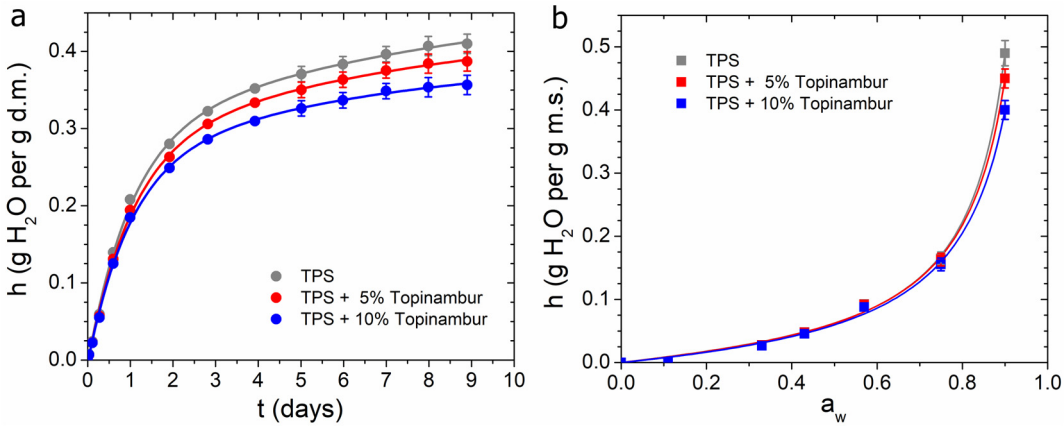

Figure 2. (**a**) Kinetics of water vapor sorption at 90% RH, presented as water content h as a function of time. (**b**) Water sorption isotherms, plotted as water content h as a function of water activity a_w. Kinetics curves were fitted with a first-order bi-exponential kinetics model (Equation (2)), and fitted parameters are shown in Table 2. Water sorption isotherms were fitted with the GAB model (Equation (3)), and fitted parameters are shown in Table 1. The error bars in the figures represent the standard deviation. The nonlinear curve fitting was performed using the standard deviations as weighting factors.

Table 1. Parameters obtained by fitting the sorption isotherms presented in Figure 2b using the Guggenheim–Anderson–De Boer (GAB) model, as described in Equation (3).

Filler Content	Water Sorption Isotherms Parameters			
	N (g per g)	c	k	R^2
0%	0.051 ± 0.008	1.55 ± 0.76	0.999 ± 0.008	0.998
5%	0.054 ± 0.009	1.43 ± 0.71	0.988 ± 0.006	0.997
10%	0.056 ± 0.011	1.29 ± 0.63	0.971 ± 0.004	0.997

Table 2. Parameters obtained from fitting the first-order bi-exponential kinetics model (Equation (2)) to the water sorption kinetics of Figure 2a.

Filler Content	Hydration Kinetics Parameters						
	h_∞ (g/g)	τ_1 (Days)	$\Delta h_1/h_\infty$	τ_2 (Days)	$\Delta h_2/h_\infty$	τ (Days)	R^2
0%	0.49 ± 0.02	1.03 ± 0.23	0.60 ± 0.02	9.1 ± 0.7	0.40 ± 0.02	4.3 ± 0.7	0.999
5%	0.45 ± 0.02	1.05 ± 0.23	0.62 ± 0.02	8.2 ±0.5	0.38 ± 0.02	3.8 ± 0.5	0.999
10%	0.40 ± 0.02	0.99 ± 0.22	0.66 ± 0.02	6.6 ± 0.4	0.36 ± 0.02	3.0 ± 0.4	0.999

Water vapor sorption isotherms provide essential insights into the interactions between water and the polymeric matrix, as well as characterizing the distribution of water within the material [19,20]. Water vapor sorption isotherms of TPS films and topinambur fiber-reinforced films are shown in Figure 2b. Table 1 displays the parameters obtained by fitting the experimental data using Equation (3). At low a_w values, the isotherms indicate limited hydration, which becomes substantially higher when $a_w > 0.6$. This behavior indicates that most hydration water molecules form multilayers, while only a minor fraction is directly bound to the polymer matrix, constituting the hydration monolayer. Such a pattern is typical of hydrophilic materials derived from biopolymers, suggesting that most of the hydration water exists as mobile water molecules [20,21]. The hydration equilibrium value at 90% RH (h_∞) and the water sorption isotherm for neat TPS film, shown in Table 2 and Figure 2b, respectively, were found to be comparable with previous studies on thermoplastic

potato starch plasticized with similar levels of glycerol and sorbitol [25]. Research on water sorption isotherms of fiber-reinforced TPS materials is still scarce. The available studies present hydration values at only one relative humidity condition [45,47,48], which restricts the understanding that could be gained from complete hydration isotherms.

From Table 1, it can be observed that the incorporation of topinambur fiber leads to a slight increase in the N parameter, suggesting a marginal rise in the amount of hydration water in the monolayer. On the other hand, a decreasing trend in the c parameter was observed with increasing fiber content, suggesting a reduced binding force of the water molecules to the polymer matrix when fibers are present in the material. Finally, a significant decrease in the k values is evident in the fiber-reinforced films, implying a reduction in the multilayer water content, which predominantly governs the overall hydration. These findings confirm that the addition of topinambur fiber decreases the hydrophilicity of the material, which is consistent with the results from the water sorption kinetics experiments. Furthermore, the incorporation of fiber tends to reduce the binding strength of water molecules to the matrix, thereby enhancing the mobility of hydration water molecules within the polymer network.

3.3. Water Vapor Transport

It has been proposed that in hydrophilic biopolymeric films with a homogeneous and continuous matrix, water transport proceeds mainly through a sorption–diffusion–desorption mechanism rather than via pore pathways [21,26]. Water vapor permeability is a crucial characteristic of biopolymer-based films, as it governs their capacity to control moisture transfer between a system and its surroundings. As the permeant water interacts with the matrix, the water vapor transport of hydrophilic films deviates from ideality, producing anomalies such as the dependence of the water vapor permeability on the thickness [21,28] and the water pressure gradient [21,27]. Therefore, to compare the experimental water vapor permeability (P_w^{exp}) values of different films, they must have the same thickness and be subjected to identical water vapor pressure gradient conditions. In our experiments, sorption occurs in the atmosphere of 90% RH and desorption in the exposed side to 10% RH. Also, in this study, all films were obtained with a constant thickness, as detailed in Table 3, to ensure that variations in P_w^{exp} are attributed solely to the composition of the material rather than differences in film thickness.

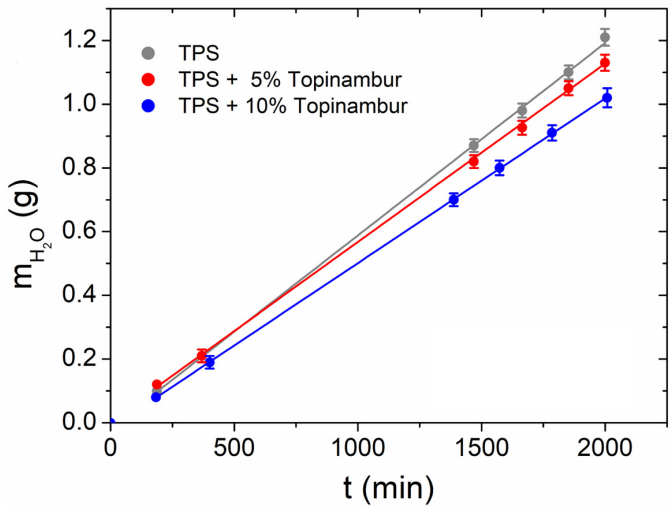

Figure 3. Experimental values of the amount of water transported m_{H_2O} as a function of time t for cassava starch films reinforced with topinambur fiber content of 5 and 10%, together with a linear fit. The error bars shown in the figures represent the standard deviation. The linear regression was carried out with the standard deviations used as weighting factors.

Table 3. Values of water vapor flux (J_w), obtained from the slope of a linear regression of weight loss versus time (Figure 3) and Equation (4), experimental water vapor permeability (P_w^{exp}), calculated according to Equation (5), and the effective diffusion (D_w^{eff}) and effective water solubility (S_w^{eff}) coefficients, calculated from Equations (7) and (8), respectively, for the three developed films. L and $\rho_{d.b.}$ refer to the thickness and density measurements of the dried film, respectively. Values sharing the same letter in a column do not differ significantly.

Filler Content	L (mm)	$\rho_{d.b.}$ (10^4 g m^{-3})	Water Transport Parameters			
			J_w (10^{-3} gs^{-1}m^{-2})	P_w^{exp} (10^{-10} gs^{-1}m^{-1}Pa^{-1})	S_w^{eff} (gm^{-3}Pa^{-1})	D_w^{eff} (10^{-13} m^2 s^{-1})
0%	0.43 ± 0.01 [a]	121 ± 6 [a]	4.60 ± 0.08 [a]	9.3 ± 0.2 [a]	281 ± 11 [a]	33 ± 2 [a]
5%	0.43 ± 0.01 [a]	123 ± 5 [a]	4.29 ± 0.03 [b]	8.7 ± 0.1 [b]	262 ± 12 [b]	33 ± 2 [a]
10%	0.43 ± 0.01 [a]	125 ± 4 [a]	3.97 ± 0.02 [c]	8.2 ± 0.1 [c]	236 ± 12 [c]	35 ± 1 [b]

Values followed by the same letter (a, b or c) within the same column are not significantly different ($p > 0.05$).

Figure 3 presents the experimental values of the amount of water transported, m_{H_2O}, as a function of time t. From these data, the slopes of straight lines representing the water transport rates $\Delta m_{H_2O}/\Delta t$ were determined as described in Section 2.3.5. Afterwards, J_w and P_w^{exp} were calculated using Equations (4) and (5), respectively. The corresponding values are reported in Table 3. It was observed from Figure 3 that the slope $\Delta m_{H_2O}/\Delta t$ was greater for the TPS film and that it decreased as the fiber content in the material increased. These results lead to a significant decrease in J_w and P_w^{exp} with increasing the fiber content in the matrix, as shown in Table 3.

The dry-basis film density $\rho_{d.b.}$, also presented in Table 3, showed no significant variation between the different formulations. $\rho_{d.b.}$ was used to calculate the effective water solubility S_w^{eff} via Equation (7), while the effective water diffusion D_w^{eff} was derived from Equation (8). All these values are summarized in Table 3, where it can be observed that S_w^{eff} decreases significantly as the topinambur fiber is incorporated into the material. It can also be seen in Table 3, that D_w^{eff} increases when the fiber is incorporated at the highest concentration studied. This result aligns with the trends observed in both water sorption kinetics and water sorption isotherms experiments, which suggest that at the highest topinambur fiber concentration tested, hydration water molecules exhibit enhanced molecular mobility and reduced binding force to the polymer matrix. Because S_w^{eff} and D_w^{eff} contribute independently to P_w^{exp}, as described by Equation (6), the observed decrease in P_w^{exp} upon fiber incorporation can be attributed primarily to the more pronounced reduction in the S_w^{eff} caused by the presence of the filler.

These results collectively demonstrate that the incorporation of topinambur fiber significantly influences the water transport properties of the TPS films. Specifically, the marked reduction in effective water solubility, rather than changes in water diffusivity, appears to be the dominant factor driving the decrease in water permeability. This behavior is consistent with a more hydrophobic matrix environment, where water–polymer interactions are weakened due to the presence of the fiber, ultimately resulting in lower water uptake and reduced overall water vapor permeability.

3.4. Surface Roughness and Contact Angle Under Varying Humidity Conditions

Beyond internal hydration behavior, surface properties such as roughness and wettability can also be affected by environmental humidity and filler content. To evaluate these effects, the surface roughness (Ra) and static contact angle of neat TPS and TPS reinforced with 5% and 10% topinambur fiber were measured after conditioning the films at 0%, 43%, and 90% relative humidity (Figure 4).

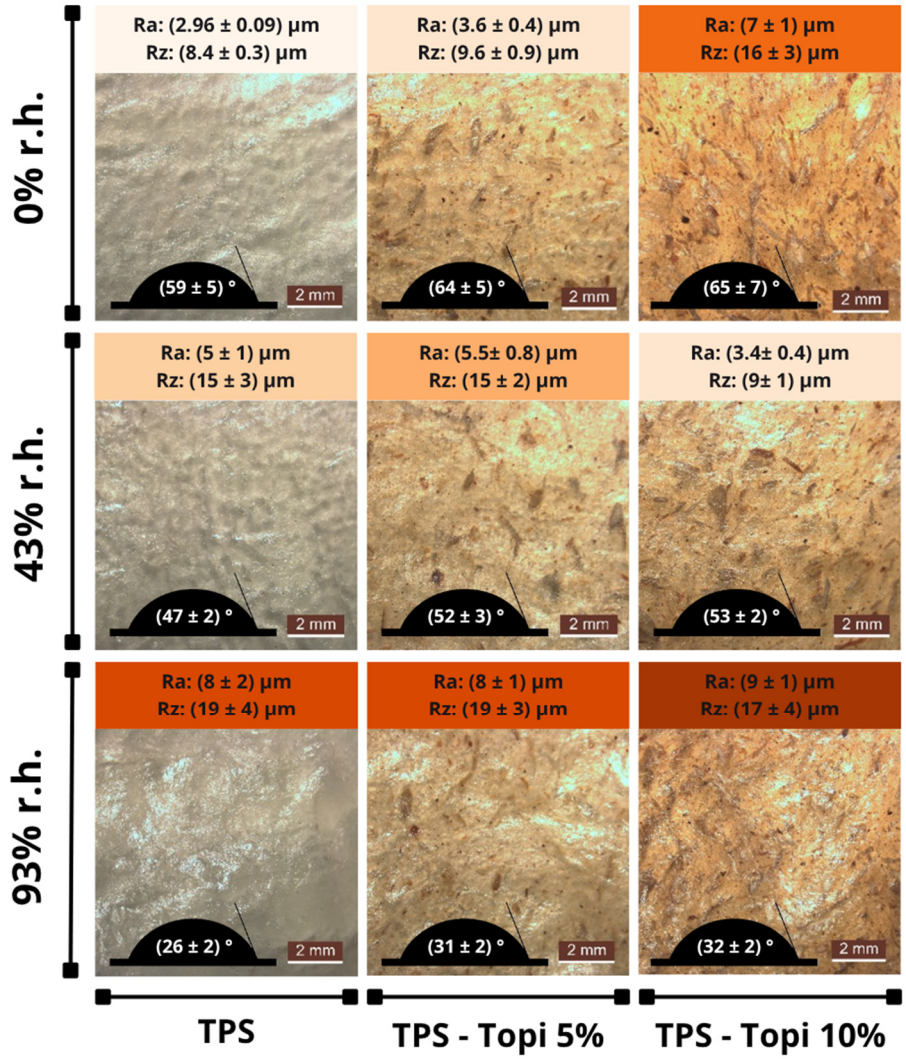

Figure 4. Optical micrographs, surface roughness parameters (Ra and Rz), and contact angle values for TPS-based films reinforced with topinambur fibers, after exposure to 0%, 43%, and 93% relative humidity. The background color of the roughness labels corresponds to the degree of surface roughness: darker colors represent higher Ra and Rz values.

As shown in Figure 4, the surface roughness of TPS and the 5% fiber composite remains relatively similar across all humidity levels. This suggests that, at this fiber concentration, the reinforcement does not exert a sufficient effect to modify the surface morphology of the material. This behavior could be related to the homogeneous distribution of fibers within the matrix at 5% fiber content, as observed in the SEM micrographs (Figure 1b), which likely prevents the formation of fiber agglomerates or surface irregularities.

Moreover, the contact angle values remain moderately high at low relative humidity and progressively decrease as RH increases, which is consistent with an increase in surface hydrophilicity resulting from the higher water content in the samples at elevated RH levels. Likewise, across all RH levels studied, the contact angles of both 5% and 10% fiber-reinforced samples are consistently higher than those of neat TPS, indicating that fiber addition improves surface water repellency.

At 0% RH ($a_w = 0$), where the water content in the films is minimal, the composite with 10% fiber exhibits a markedly higher surface roughness than the neat TPS. TPS-TOPI10% reached an Ra of (7 ± 1) µm and a contact angle of (65 ± 7)°, while the neat TPS showed an Ra of (2.96 ± 0.09) µm and a contact angle of (59 ± 5)°. This represents an increase of approximately 140% in surface roughness and about 10% in contact angle, confirming the

enhanced hydrophobicity and surface texturing of the fiber-reinforced composite under dry conditions. This increase may be attributed to the presence of randomly oriented fiber agglomerates on the surface, generating irregularities that contribute to roughness enhancement. Similar behavior has been reported by other authors [49] in thermoplastic corn starch films reinforced with fibrous residues, where the disorganized fiber distribution at the surface led to increased surface roughness as observed by atomic force microscopy.

The data obtained at 10% RH (a_w = 0.1) were included in the analysis due to their relevance. Despite minimal water absorption (~1 wt%), the TPS film shows increased roughness (Ra = 4.3 ± 0.3 μm), while the 10% fiber composite exhibits a decrease (Ra = 3.2 ± 0.4 μm), reversing the trend observed at 0% RH. This opposing trend may be attributed to the biphasic nature of TPS, in which water interacts differently with the plasticizer-rich and starch-rich phases. The absorbed water can promote phase reorganization: in the neat matrix, it may enhance retrogradation and surface deformation, whereas in the reinforced composite, fiber–matrix interactions appear to buffer these effects. The contact angle at this RH level decreased slightly to (53 ± 2)° in TPS and (62 ± 3)° in TPS-TOPI10%, maintaining a relative increase of ~17%. These results again support the improved water barrier effect provided by fiber addition.

Specifically, the literature suggests that plasticizers tend to migrate toward the fiber–matrix interface in hydrophilic composites, forming interfacial regions enriched in plasticizer [50–52]. Small amounts of water absorbed in this region may act as secondary plasticizers, helping to relieve internal stresses and promoting a smoother surface through improved phase integration. Additionally, the fibers can serve as anchors that restrict phase separation and structural rearrangement, contributing further to surface stabilization.

At high RH (a_w = 0.9), surface roughness increases for all formulations. TPS exhibited an Ra of (8 ± 2) μm, while TPS-TOPI10% reached (9 ± 1) μm. This may be due to additional water uptake by the lignocellulosic fibers, which can swell or deform, leading to increased surface texturing. In neat TPS, the moisture likely promotes phase separation or starch retrogradation, resulting in surface instability. The contact angle values at this RH level is significantly lower in all samples, but the 10% fiber composite retains a slightly higher angle (~32° vs. 26° in neat TPS), indicating partial retention of hydrophobic surface character despite strong moisture exposure.

The systematic evaluation of how relative humidity affects the surface roughness of TPS-based biocomposites by contact profilometry has not been previously reported. In addition, by integrating contact angle measurements under identical conditioning, we provide a complementary perspective on the relationship between surface texture and wettability. These results demonstrate that topinambur fiber not only influences the internal hydration behavior of TPS films but also plays a key role in modifying their surface morphology and hydrophobicity under varying humidity conditions.

3.5. FTIR Analysis and Evidence of Molecular Interactions

FTIR spectroscopy was employed to study the interaction between thermoplastic starch and topinambur fiber. In the FTIR spectrum of the thermoplastic starch Figure 5a, the region between 3000–3600 cm^{-1} was associated with the stretching of hydroxyl groups (-OH). The band at 2800 cm^{-1} were attributed to C-H stretching vibrations. The band around 1640 cm^{-1} has been associated with the bending of O-H in adsorbed water. Bands in the range of 1400 and 1450 cm^{-1} correspond to O-H bonding. The absorption in the ranges 950–1020 cm^{-1} and 1070–1155 cm^{-1} is associated with C–O stretching, specifically from the C–OC linkage within the anhydroglucose unit and from the C–OH functionality [53,54].

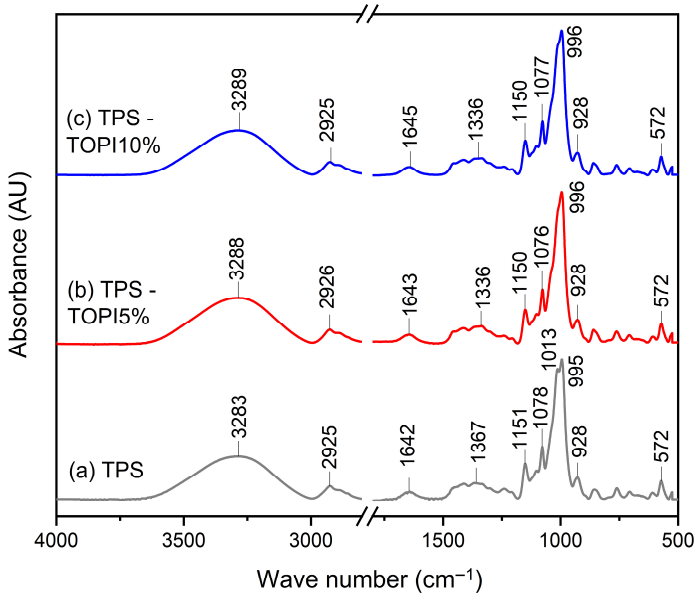

Figure 5. FTIR spectrum of: (**a**) thermoplastic starch and the starch biocomposites with (**b**) 5 and (**c**) 10 wt% of topinambur fiber.

The FTIR peaks of the biocomposites are observed at almost identical positions as those in the TPS (Figure 5b,c), showing the compatibility between the matrix and the fiber. This similarity can be explained by the fact that starch and lignocellulosic fibers have a common basic chemical composition, with cellulose as the primary structural component [44,55]. Whereas the O-H stretching band in the starch biocomposites shows a shift to a higher wavenumber. This might indicate new formation of hydrogen bonds between the hydroxyl groups present in starch, plasticizers and the fiber. The formation of these interactions improved the water resistance of the biocomposites.

In this region, it is also possible to estimate the ratio between the amorphous and crystalline fractions of starch-based films. Several authors [56,57] have highlighted a relationship between the relative absorbance intensities of the peaks at 1047 cm^{-1} (associated with more ordered or crystalline starch) and 1022 cm^{-1} (representing amorphous starch regions)—i.e., the 1047/1022 cm^{-1} band ratio—and the degree of crystallinity in starch samples. In particular, when comparing TPS films and films reinforced with 5% and 10% topinambur fiber, the crystallinity ratio was higher in the fiber-containing materials, exceeding that of the neat starch-based film by 12% and 10%, respectively. However, these results should be interpreted with caution, as not only starch but also components of the parenchymal tissue present in the *Helianthus tuberosus* fiber may contribute to the absorbance in this spectral region, potentially affecting starch crystallinity estimations [58,59]. To further clarify this point, X-ray scattering analysis was performed. Figure 6. shows SAXS/WAXS data corresponding to the TPS and biocomposite films. All samples exhibited the characteristic broad peaks of cassava starch-based TPS, centered around $2\theta \approx 17^\circ$ and 22°, which correspond to the typical B-type diffraction pattern [60]. The addition of topinambur fibers did not generate additional crystalline peaks, suggesting that no new crystalline phases were formed. However, an increase in peak intensity was observed in the biocomposites compared to neat TPS. This effect suggests that the higher crystallinity contribution arises from the cellulose structure present in the fibers rather than from rearrangements in the TPS matrix. The incorporation of 5 wt% fibers led to a clear increase in crystallinity, which can be attributed to both the intrinsic crystalline domains of cellulose and to the possible nucleating effect of the fibers that promote some ordering in the TPS matrix. In contrast, when the fiber content was increased to 10 wt%, the crystallinity, although still higher

than that of neat TPS, decreased compared to the 5 wt% composite. This reduction may be related to stronger fiber–matrix interactions that restrict the rearrangement of starch chains, thus limiting further ordering. Similar behaviors have been reported in starch-based biocomposites [54,61,62], where fiber addition led to an increase in crystallinity, particularly reflected in the enhanced intensity of the diffraction peak at $2\theta \approx 22^{\circ}$, which evidences the contribution of cellulose domains within the materials.

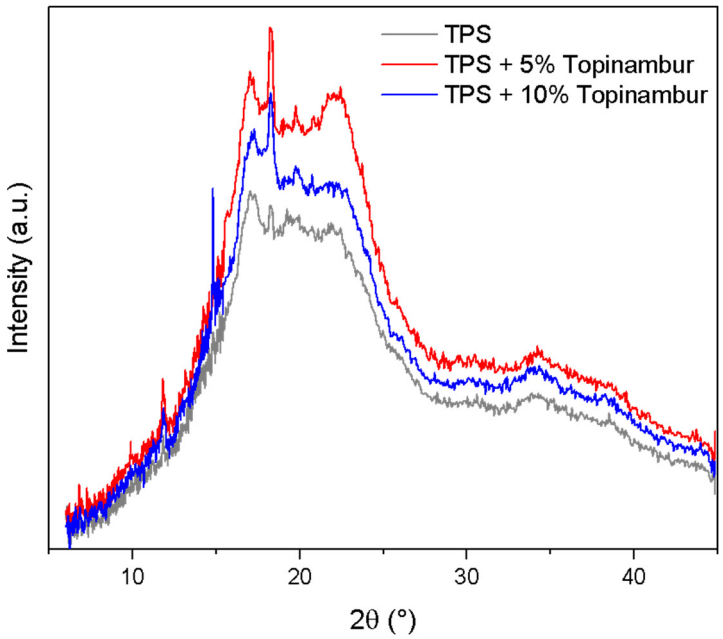

Figure 6. SAXS/WAXS patterns of TPS and TPS biocomposites containing 5% and 10 wt% topinambur fiber.

In summary, FTIR analysis suggests that topinambur fiber interacts with the TPS matrix, as indicated by subtle spectral variations. This interpretation is consistent with SEM observations of fiber integration and with X-ray scattering results showing changes in structural order, together supporting the improvements in moisture barrier properties.

4. Conclusions

This study demonstrated, for the first time, that the incorporation of fibers derived from the aerial part of *Helianthus tuberosus* into TPS films significantly modulates their water-related behavior and surface properties. The addition of topinambur fibers decreased the hydration and, consequently, the effective water solubility within the films. It is the pronounced reduction in effective water solubility, rather than the slight increase in water diffusivity, that predominantly governs the observed decrease in water vapor permeability. These results suggest an overall enhancement in hydrophobicity and water vapor barrier properties induced by fiber incorporation. Moreover, morphological analysis revealed that fiber content influences the surface response of TPS films to environmental humidity. While films with low fiber content showed minimal changes, those containing 10% fiber exhibited humidity-dependent variations in surface roughness, suggesting alterations in internal stress relaxation and fiber–matrix interactions.

Beyond the reduction in hydration and vapor permeability, the ability to capture humidity-induced morphological changes using surface profilometry represents a novel contribution to the field. These findings deepen the understanding of structure–property relationships in starch-based biocomposites and open new avenues for tailoring surface behavior in environmentally sensitive applications.

Overall, the valorization of topinambur agro-industrial residues as natural filler in TPS films emerges as an effective and sustainable strategy to improve moisture barrier properties. These findings are particularly relevant for applications in sustainable agriculture and bio-based packaging, where control over water transport and environmental response is critical. Future studies will focus on assessing the long-term stability and biodegradability of these materials under field conditions.

Author Contributions: Conceptualization, M.C.L., M.A.G., A.G.S. and L.R.; Data curation, L.F.S.M. and A.G.S.; Formal analysis, L.F.S.M., M.C.L., M.A.G., A.G.S. and L.R.; Funding acquisition, M.A.G., A.G.S. and L.R.; Investigation, L.F.S.M., M.C.L. and A.G.S.; Methodology, L.F.S.M., M.C.L., M.A.G., A.G.S. and L.R.; Project administration, M.A.G., A.G.S. and L.R.; Resources, M.C.L., M.A.G., A.G.S. and L.R.; Software, L.F.S.M. and A.G.S.; Supervision, M.A.G., A.G.S. and L.R.; Validation, M.A.G., A.G.S. and L.R.; Visualization, L.F.S.M., A.G.S. and L.R.; Writing—original draft, L.F.S.M. and A.G.S.; Writing—review & editing, M.A.G., A.G.S. and L.R. All authors have read and agreed to the published version of the manuscript.

Funding: This research was funded by Agencia Nacional de Promoción Científica y Tecnológica (ANPCyT), grant numbers: PICTA 2021-0095, PICT 2019-3843 and PICT 2019-2827; CONICET, grant number: PIP 112202101 00785CO and Universidad de Buenos Aires, grant number: UBACYT 20020170100381BA, of Argentina.

Data Availability Statement: The data presented in this study are available on request from the corresponding author. The data are not publicly available due to the ongoing use of the dataset in related research.

Acknowledgments: Conventional powder diffraction and SAXS/WAXS studies were performed at the Laboratorio de Cristalografía Aplicada, ITECA institute, CONICET-Universidad Nacional de San Martín, Argentina. We thank Diego G. Lamas (ITECA) for these measurements and useful discussions.

Conflicts of Interest: The authors declare no conflicts of interest. The funders had no role in the design of the study; in the collection, analyses, or interpretation of data; in the writing of the manuscript; or in the decision to publish the results.

Abbreviations

The following abbreviations are used in this manuscript:

TPS	Thermoplastic starch
PE	Polyethylene
PP	Polypropylene
PS	Polystyrene
ASTM	American Standard for Testing Materials
FTIR	Fourier Transform Infrared Spectroscopy
SEM	Scanning Electron Microscopy
GAB	Guggenheim–Anderson–De Boer model
WVP	Water vapor permeability
RH	Relative humidity
DM	Dried mass
a_w	Water activity

References

1. Cheng, J.; Gao, R.; Zhu, Y.; Lin, Q. Applications of biodegradable materials in food packaging: A review. *Alex. Eng. J.* **2024**, *91*, 70–83. [CrossRef]
2. Lackner, M.; Mukherjee, A.; Koller, M. What Are "Bioplastics"? Defining Renewability, Biosynthesis, Biodegradability, and Biocompatibility. *Polymers* **2023**, *15*, 4695. [CrossRef]

3. Campanale, C.; Galafassi, S.; Di Pippo, F.; Pojar, I.; Massarelli, C.; Uricchio, V.F. A critical review of biodegradable plastic mulch films in agriculture: Definitions, scientific background and potential impacts. *TrAC Trends Anal. Chem.* **2024**, *170*, 117391. [CrossRef]
4. Thrän, J.; Garcia-Garcia, G.; Parra-López, C.; Ufarte, A.; García-García, C.; Parra, S.; Sayadi-Gmada, S. Environmental and economic assessment of biodegradable and compostable alternatives for plastic materials in greenhouses. *Waste Manag.* **2024**, *175*, 92–100. [CrossRef] [PubMed]
5. Cao, X.; Liang, Y.; Jiang, J.; Mo, A.; He, D. Organic additives in agricultural plastics and their impacts on soil ecosystems: Compared with conventional and biodegradable plastics. *TrAC Trends Anal. Chem.* **2023**, *166*, 117212. [CrossRef]
6. Flury, M.; Narayan, R. Biodegradable plastic as an integral part of the solution to plastic waste pollution of the environment. *Curr. Opin. Green Sustain. Chem.* **2021**, *30*, 100490. [CrossRef]
7. Thacharodi, A.; Meenatchi, R.; Hassan, S.; Hussain, N.; Bhat, M.A.; Arockiaraj, J.; Ngo, H.H.; Le, Q.H.; Pugazhendhi, A. Microplastics in the environment: A critical overview on its fate, toxicity, implications, management, and bioremediation strategies. *J. Environ. Manag.* **2024**, *349*, 119433. [CrossRef]
8. Sanyang, M.L.; Sapuan, S.M. Thermoplastic Starch: A Potential Biodegradable Polymer for Food Packaging Applications. *Fibers* **2019**, *7*, 32. [CrossRef]
9. Rivadeneira-Velasco, K.E.; Utreras-Silva, C.A.; Díaz-Barrios, A.; Sommer-Márquez, A.E.; Tafur, J.P.; Michell, R.M. Green Nanocomposites Based on Thermoplastic Starch: A Review. *Polymers* **2021**, *13*, 3227. [CrossRef]
10. Ribba, L.; Garcia, N.L.; D'Accorso, N.; Goyanes, S. Disadvantages of Starch-Based Materials, Feasible Alternatives in Order to Overcome These Limitations. In *Starch-Based Materials in Food Packaging: Processing, Characterization and Applications*; Villar, M.A., Barbosa, S.E., García, M.A., Castillo, L.A., López, O.V., Eds.; Academic Press: Cambridge, MA, USA, 2018; pp. 154–196. [CrossRef]
11. Liu, F.; Ren, J.; Yang, Q.; Zhang, Q.; Zhang, Y.; Xiao, X.; Cao, Y. Improving water resistance and mechanical properties of starch-based films by incorporating microcrystalline cellulose in a dynamic network structure. *Int. J. Biol. Macromol.* **2024**, *260*, 129404. [CrossRef] [PubMed]
12. Asrofi, M.; Abral, H.; Kasim, A.; Pratoto, A.; Mahardika, M.; Hafizulhaq, F. Mechanical Properties of a Water Hyacinth Nanofiber Cellulose Reinforced Thermoplastic Starch Bionanocomposite: Effect of Ultrasonic Vibration During Processing. *Fibers* **2018**, *6*, 40. [CrossRef]
13. Díaz, A.; García, M.A.; Dini, C. Jerusalem artichoke flour as food ingredient and as source of fructooligosaccharides and inulin. *J. Food Compos. Anal.* **2022**, *114*, 104863. [CrossRef]
14. De Santis, D.; Frangipane, M.T. Evaluation of chemical composition and sensory profile in Jerusalem artichoke (*Helianthus tuberosus* L.) tubers: The effect of clones and cooking conditions. *Int. J. Gastron. Food Sci.* **2018**, *11*, 25–30. [CrossRef]
15. Sierra Montes, L.F.; Melaj, M.A.; Lorenzo, M.C.; Ribba, L.; García, M.A. Biodegradable Composite Materials Based on Cassava Starch and Reinforced with Topinambur (*Helianthus tuberosus*) Aerial Part Fiber. *Sust. Polym. Energy* **2024**, *2*, 10004. [CrossRef]
16. Cazón, P.; Velázquez, G.; Vázquez, M. Regenerated cellulose films combined with glycerol and polyvinyl alcohol: Effect of moisture content on the physical properties. *Food Hydrocoll.* **2020**, *103*, 105657. [CrossRef]
17. Coma, M.E.; Peltzer, M.A.; Delgado, J.F.; Salvay, A.G. Water kefir grains as an innovative source of materials: Study of plasticiser content on film properties. *Eur. Polym. J.* **2019**, *120*, 109234. [CrossRef]
18. Perotto, G.; Simonutti, R.; Ceseracciu, L.; Mauri, M.; Besghini, D.; Athanassiou, A. Water-induced plasticization in vegetable-based bioplastic films: A structural and thermo-mechanical study. *Polymer* **2020**, *200*, 122598. [CrossRef]
19. Guggenheim, E.A. *Applications of Statistical Mechanics*; Oxford University Press: Oxford, UK, 1966.
20. Bertuzzi, M.A.; Castro Vidaurre, E.F.; Armada, M.; Gottifredi, J.C. Water vapor permeability of edible starch based films. *J. Food. Eng.* **2007**, *80*, 972–978. [CrossRef]
21. Delgado, J.F.; Peltzer, M.A.; Salvay, A.G. Water Vapour Transport in Biopolymeric Materials: Effects of Thickness and Water Vapour Pressure Gradient on Yeast Biomass-Based Films. *J. Polym. Environ.* **2022**, *30*, 2976–2989. [CrossRef]
22. Cuq, B.; Gontard, N.; Aymard, C.; Guilbert, S. Relative humidity and temperature effects on mechanical and water vapor barrier properties of myofibrillar protein-based films. *Polym. Gels Netw.* **1997**, *5*, 1–15. [CrossRef]
23. Guillard, V.; Broyart, B.; Bonazzi, C.; Guilbert, S.; Gontard, N. Preventing Moisture Transfer in a Composite Food Using Edible Films: Experimental and Mathematical Study. *J. Food Sci.* **2003**, *68*, 2267–2277. [CrossRef]
24. Angellier-Coussy, H.; Gastaldi, E.; Gontard, N.; Guillard, V. Influence of processing temperature on the water vapour transport properties of wheat gluten based agromaterials. *Ind. Crops Prod.* **2011**, *33*, 457–461. [CrossRef]
25. Díaz-Díaz, E.D.; Ribba, L.; Makovec, J.; Melaj, M.; Bernal, C.; Goyanes, S.; Salvay, A.G. Development of Biodegradable Films for Sustainable Agricultural Applications by Using Thermoplastic Potato Starch and PBAT. *J. Appl. Polym. Sci.* **2025**, *142*, e57685. [CrossRef]
26. Rogers, C.E. Permeation of Gases and Vapours in Polymers. In *Polymer Permeability*; Comyn, J., Ed.; Springer: Dordrecht, The Netherlands, 1985; pp. 11–73. [CrossRef]

27. Roy, S.; Gennadios, A.; Weller, C.L.; Testin, R.F. Water vapor transport parameters of a cast wheat gluten film. *Ind. Crops Prod.* **2000**, *11*, 43–50. [CrossRef]
28. Delgado, J.F.; Peltzer, M.A.; Wagner, J.R.; Salvay, A.G. Hydration and water vapour transport properties in yeast biomass based films: A study of plasticizer content and thickness effects. *Eur. Polym. J.* **2018**, *99*, 9–17. [CrossRef]
29. Cuq, B.; Gontard, N.; Cuq, J.L.; Guilbert, S. Functional Properties of Myofibrillar Protein-based Biopackaging as Affected by Film Thickness. *J. Food. Sci.* **1996**, *61*, 580–584. [CrossRef]
30. Park, H.J.; Weller, C.L.; Vergano, P.J.; Testin, R.F. Permeability and Mechanical Properties of Cellulose-Based Edible Films. *J. Food Sci.* **1993**, *58*, 1361–1364. [CrossRef]
31. Pereda, M.; Aranguren, M.I.; Marcovich, N.E. Water vapor absorption and permeability of films based on chitosan and sodium caseinate. *J. Appl. Polym. Sci.* **2009**, *111*, 2777–2784. [CrossRef]
32. Balaguer, M.P.; Cerisuelo, J.P.; Gavara, R.; Hernandez-Muñoz, P. Mass transport properties of gliadin films: Effect of cross-linking degree, relative humidity, and temperature. *J. Memb. Sci.* **2013**, *428*, 380–392. [CrossRef]
33. Cuq, B.; Gontard, N.; Cuq, J.L.; Guilbert, S. Selected Functional Properties of Fish Myofibrillar Protein-Based Films As Affected by Hydrophilic Plasticizers. *J. Agric. Food Chem.* **1997**, *45*, 622–626. [CrossRef]
34. Turhan, K.N.; Şahbaz, F. Water vapor permeability, tensile properties and solubility of methylcellulose-based edible films. *J. Food Eng.* **2004**, *61*, 459–466. [CrossRef]
35. Nascimento, P.; Marim, R.; Carvalho, G.; Mali, S. Nanocellulose Produced from Rice Hulls and its Effect on the Properties of Biodegradable Starch Films. *Mater. Res.* **2016**, *19*, 167–174. [CrossRef]
36. Delgado, J.F.; de la Osa, O.; Salvay, A.G.; Cavallo, E.; Cerrutti, P.; Foresti, M.L.; Peltzer, M.A. Reinforcement of Yeast Biomass Films with Bacterial Cellulose and Rice Husk Cellulose Nanofibres. *J. Polym. Environ.* **2021**, *29*, 3242–3251. [CrossRef]
37. Pongsuwan, C.; Boonsuk, P.; Sermwittayawong, D.; Aiemcharoen, P.; Mayakun, J.; Kaewtatip, K. Banana inflorescence waste fiber: An effective filler for starch-based bioplastics. *Ind. Crops Prod.* **2022**, *180*, 114731. [CrossRef]
38. Averous, L.; Boquillon, N. Biocomposites based on plasticized starch: Thermal and mechanical behaviours. *Carbohydr. Polym.* **2004**, *56*, 111–122. [CrossRef]
39. Campos, A.; Sena Neto, A.R.; Rodrigues, V.B.; Luchesi, B.R.; Mattoso, L.H.C.; Marconcini, J.M. Effect of raw and chemically treated oil palm mesocarp fibers on thermoplastic cassava starch properties. *Ind. Crops Prod.* **2018**, *124*, 149–154. [CrossRef]
40. Cantor, C.R.; Schimmel, P.R. *Biophysical Chemistry: Part III: The Behavior of Biological Macromolecules*; W. H. Freeman: San Francisco, CA, USA, 1980.
41. De La Cruz, G.V.; Torres, J.A.; Martín-Polo, M.O. Temperature effect on the moisture sorption isotherms for methylcellulose and ethylcellulose films. *J. Food Eng.* **2001**, *48*, 91–94. [CrossRef]
42. *ASTM-E96 2016*; Standard Test Methods for Water Vapor Transmission of Materials. ASTM International: West Conshohocken, PA, USA, 2016. [CrossRef]
43. Ladetto, M.F.; Ancarola, M.E.; Lamas, D.G.; Kollrich, B.A.; Cucher, M.A.; Álvarez, V.A.; Glisoni, R.J.; Castro, G.R.; Islan, G.A.; Cuestas, M.L. Enhanced antifungal efficacy of clotrimazole and itraconazole delivered via solid lipid nanoparticles for potential otomycosis therapy. *J. Drug Deliv. Sci. Technol.* **2025**, *113*, 107401. [CrossRef]
44. Kaewtatip, K.; Thongmee, J. Studies on the structure and properties of thermoplastic starch/luffa fiber composites. *Mater. Des.* **2012**, *40*, 314–318. [CrossRef]
45. Ma, X.; Yu, J.; Kennedy, J.F. Studies on the properties of natural fibers-reinforced thermoplastic starch composites. *Carbohydr. Polym.* **2005**, *62*, 19–24. [CrossRef]
46. Bénézet, J.C.; Stanojlovic-Davidovic, A.; Bergeret, A.; Ferry, L.; Crespy, A. Mechanical and physical properties of expanded starch, reinforced by natural fibres. *Ind. Crops Prod.* **2012**, *37*, 435–440. [CrossRef]
47. Vallejos, M.E.; Curvelo, A.A.S.; Teixeira, E.M.; Mendes, F.M.; Carvalho, A.J.F.; Felissia, F.E.; Area, M.C. Composite materials of thermoplastic starch and fibers from the ethanol–water fractionation of bagasse. *Ind. Crops Prod.* **2011**, *33*, 739–746. [CrossRef]
48. Gironès, J.; López, J.P.; Mutjé, P.; Carvalho, A.J.F.; Curvelo, A.A.S.; Vilaseca, F. Natural fiber-reinforced thermoplastic starch composites obtained by melt processing. *Compos. Sci. Technol.* **2012**, *72*, 858–863. [CrossRef]
49. López, O.V.; Versino, F.; Villar, M.A.; García, M.A. Agro-industrial residue from starch extraction of *Pachyrhizus ahipa* as filler of thermoplastic corn starch films. *Carbohydr. Polym.* **2015**, *134*, 324–332. [CrossRef]
50. Aouada, F.A.; Mattoso, L.H.C.; Longo, E. Enhanced bulk and superficial hydrophobicities of starch-based bionanocomposites by addition of clay. *Ind. Crops Prod.* **2013**, *50*, 449–455. [CrossRef]
51. Spiridon, I.; Teacă, C.A.; Bodîrlău, R.; Bercea, M. Behavior of Cellulose Reinforced Cross-Linked Starch Composite Films Made with Tartaric Acid Modified Starch Microparticles. *J. Polym. Environ.* **2013**, *21*, 431–440. [CrossRef]
52. Cao, X.; Chen, Y.; Chang, P.R.; Stumborg, M.; Huneault, M.A. Green composites reinforced with hemp nanocrystals in plasticized starch. *J. Appl. Polym. Sci.* **2008**, *109*, 3804–3810. [CrossRef]
53. Das, S.; Basak, S.; Baite, H.; Bhowmick, M.; Debnath, S.; Roy, A.N. Jute fibre reinforced biodegradable composites using starch as a biological macromolecule: Fabrication and performance evaluation. *Int. J. Biol. Macromol.* **2024**, *273*, 132641. [CrossRef]

54. Hafizulhaq, F.; Abral, H.; Kasim, A.; Arief, S.; Affi, J. Moisture Absorption and Opacity of Starch-Based Biocomposites Reinforced with Cellulose Fiber from Bengkoang. *Fibers* **2018**, *6*, 62. [CrossRef]
55. Wani, S.A.; Kumar, P. Moisture sorption isotherms and evaluation of quality changes in extruded snacks during storage. *LWT* **2016**, *74*, 448–455. [CrossRef]
56. van Soest, J.J.G.; Tournois, H.; de Wit, D.; Vliegenthart, J.F.G. Short-range structure in (partially) crystalline potato starch determined with attenuated total reflectance Fourier-transform IR spectroscopy. *Carbohydr. Res.* **1995**, *279*, 201–214. [CrossRef]
57. Rubens, P.; Snauwaert, J.; Heremans, K.; Stute, R. In situ observation of pressure-induced gelation of starches studied with FTIR in the diamond anvil cell. *Carbohydr. Polym.* **1999**, *39*, 231–235. [CrossRef]
58. Dalmis, R. Description of a new cellulosic natural fiber extracted from *Helianthus tuberosus* L. as a composite reinforcement material. *Physiol. Plant.* **2023**, *175*, e13960. [CrossRef] [PubMed]
59. Chamorro, A.F.; Palencia, M.; Lerma, T.A. Physicochemical Characterization and Properties of Cassava Starch: A Review. *Polymers* **2025**, *17*, 1663. [CrossRef] [PubMed]
60. Zobel, H.F. Starch Crystal Transformations and Their Industrial Importance. *Starch–Stärke* **1988**, *40*, 1–7. [CrossRef]
61. Abral, H.; Dalimunthe, M.H.; Hartono, J.; Efendi, R.P.; Asrofi, M.; Sugiarti, E.; Sapuan, S.M.; Park, J.W.; Kim, H.J. Characterization of Tapioca Starch Biopolymer Composites Reinforced with Micro Scale Water Hyacinth Fibers. *Starch–Stärke* **2018**, *70*, 1700287. [CrossRef]
62. Ek, P.; Gu, B.J.; Saunders, S.R.; Huber, K.; Ganjyal, G.M. Exploration of physicochemical properties and molecular interactions between cellulose and high-amylose cornstarch during extrusion processing. *Curr. Res. Food Sci.* **2021**, *4*, 588–597. [CrossRef]

Disclaimer/Publisher's Note: The statements, opinions and data contained in all publications are solely those of the individual author(s) and contributor(s) and not of MDPI and/or the editor(s). MDPI and/or the editor(s) disclaim responsibility for any injury to people or property resulting from any ideas, methods, instructions or products referred to in the content.